Oxygen isotopic alteration in Ca-Al-rich inclusions from Efremovka: Nebular or parent body setting?

T. J. FAGAN,[1†*] A. N. KROT,[2] K. KEIL,[2] and H. YURIMOTO[1]

[1]Department of Earth and Planetary Sciences, Tokyo Institute of Technology, 2–12–1 Ookayama, Meguro, Tokyo 152–8551, Japan
[2]Hawai'i Institute of Geophysics and Planetology, School of Ocean and Earth Science and Technology,
University of Hawai'i at Manoa, Honolulu, Hawai'i 96822, USA
[†]Present address: U.S. National Museum of Natural History, Smithsonian Institution, Washington, D.C., USA
[*]Corresponding author. E-mail: fagan.tim@nmnh.si.edu

Abstract–In situ SIMS oxygen isotope data were collected from a coarse-grained type B1 Ca-Al-rich inclusion (CAI) and an adjacent fine-grained CAI in the reduced CV3 Efremovka to evaluate the timing of isotopic alteration of these two objects. The coarse-grained CAI (CGI-10) is a sub-spherical object composed of elongate, euhedral, normally-zoned melilite crystals ranging up to several hundreds of μm in length, coarse-grained anorthite and Al, Ti-diopside (fassaite), all with fine-grained (~10 μm across) inclusions of spinel. Similar to many previously examined coarse-grained CAIs from CV chondrites, spinel and fassaite are ^{16}O-rich and melilite is ^{16}O-poor, but in contrast to many previous results, anorthite is ^{16}O-rich. Isotopic composition does not vary with textural setting in the CAI: analyses of melilite from the core and mantle and analyses from a variety of major element compositions yield consistent ^{16}O-poor compositions. CGI-10 originated in an ^{16}O-rich environment, and subsequent alteration resulted in complete isotopic exchange in melilite. The fine-grained CAI (FGI-12) also preserves evidence of a 1st-generation origin in an ^{16}O-rich setting but underwent less severe isotopic alteration. FGI-12 is composed of spinel ± melilite nodules linked by a mass of Al-diopside and minor forsterite along the CAI rim. All minerals are very fine-grained (<5 μm) with no apparent igneous textures or zoning. Spinel, Al-diopside, and forsterite are ^{16}O-rich, while melilite is variably depleted in ^{16}O ($\delta^{17, 18}O$ from ~−40‰ to −5‰).

The contrast in isotopic distributions in CGI-10 and FGI-12 is opposite to the pattern that would result from simultaneous alteration: the object with finer-grained melilite and a greater surface area/volume has undergone less isotopic exchange than the coarser-grained object. Thus, the two CAIs were altered in different settings. As the CAIs are adjacent to each other in the meteorite, isotopic exchange in CGI-10 must have preceded incorporation of this CAI in the Efremovka parent body. This supports a nebular setting for isotopic alteration of the commonly observed ^{16}O-poor melilite in coarse-grained CAIs from CV chondrites.

INTRODUCTION

Most refractory Ca-Al-rich inclusions (CAIs) have ^{16}O-rich isotopic compositions ($\delta^{17, 18}O$ ~−40‰, $\Delta^{17}O$ ~−20‰) that are distinct from other early solar system materials preserved in chondritic meteorites (Clayton et al. 1973; Clayton 1993). These anomalous compositions cannot be accounted for by standard mass dependent fractionation and require the presence of an anomalous oxygen reservoir of nucleosynthetic origin or mass independent fractionations before the formation of CAIs in the early solar system (Clayton et al. 1973; Thiemens 1999; Scott and Krot 2001;

Clayton 2002; Yurimoto and Kuramoto 2002; Young and Lyons 2003).

A common exception to the ^{16}O-rich composition associated with most CAI phases is melilite in the coarse-grained CAIs found in Allende and other CV3 chondrites. Melilite in the coarse-grained type B inclusions typically has ^{16}O-poor compositions of $\delta^{17, 18}O$ ~0‰, distinct from coexisting ^{16}O-rich spinel and Al, Ti-diopside (fassaite) (Clayton et al. 1977; Clayton 1993). Anorthite, the other major phase of coarse-grained type B CAIs, has been identified with relatively ^{16}O-poor isotopic compositions, though perhaps not quite as ^{16}O-depleted as melilite (Clayton

et al. 1977; Mayeda et al. 1986; Yurimoto et al. 1994). Therefore, in detail, the coarse-grained CAIs typical of CV chondrites record a complex oxygen isotopic evolution.

With the discovery that Allende and other CV chondrites have undergone metamorphism and alteration on their parent bodies (McSween 1977; Kojima et al. 1993; Krot et al. 1998), it is important to consider the possible role of parent body processes on oxygen isotopic evolution of CAIs in the CV chondrites. The possible role of parent body alteration is particularly relevant in light of recent studies that correlate progressive isotopic alteration of melilite with metamorphic grade in the CO chondrites (Wasson et al. 2001) and document the role of hydrothermal parent body alteration in redistributing O isotopes in an amoeboid olivine aggregate from Allende (Imai and Yurimoto 2003).

In this study, we evaluate the setting of isotopic alteration by comparing the distribution of oxygen isotopes in a fine-grained CAI with an adjacent coarse-grained CAI in the reduced CV3 Efremovka. Melilite is present in both of these objects but with a large contrast in grain size. If both CAIs underwent isotopic exchange on the parent body, the fine-grained melilite grains should exhibit more complete isotopic re-equilibration because of their greater surface area/volume ratio. In contrast, a more complete re-equilibration of the coarse-grained CAI would conflict with a parent body setting for isotopic exchange.

ANALYTICAL METHODS

Petrography and Mineral Compositions

A coarse-grained CAI (CGI-10) and fine-grained CAI (FGI-12) were found adjacent to each other in a polished thin section of Efremovka (E36, on loan from Dr. J. Goswami). The textures and mineralogy of the CAIs were studied by standard petrographic methods, imaging in backscattered (BSE) and secondary (SE) electrons, elemental mapping, and quantitative elemental analyses. Backscattered and SE imaging were conducted using a JEOL JSM-5310LV scanning electron microscope with an Oxford LINK-ISIS EDS detector at the Tokyo Institute of Technology (TiTech). Large-scale elemental maps of the two CAIs in Mg, Al, Ca, Si, and TiKα were collected using a focused 100 nA beam in a Cameca SX-50 electron microprobe at the University of Hawai'i (UH). Quantitative elemental analyses by energy dispersive spectroscopy (EDS) were determined using an Oxford LINK-ISIS detector attached to the JEOL JSM-5310LV SEM at TiTech. The EDS analyses were collected using a 1 nA, 15 KeV, focused (diameter ~1 μm) beam, counting for 100 sec, with a dead-time correction. Even with the focused beam, some of our EDS analyses from FGI-12 were apparently affected by beam overlap with adjacent phases. Elemental analyses by wavelength dispersive spectroscopy (WDS) were determined using a JEOL JXA-

8800 electron microprobe at TiTech under the following conditions: 15 keV, 1 μm spot-size, 12 nA, and peak and background counting times of 12–30 sec. Well-characterized oxides and silicates were used as standards for WDS.

Ion Microprobe Analyses

In situ oxygen isotope analyses were conducted using a modified Cameca 1270 ion microprobe at TiTech. A primary ion beam of mass filtered positive Cs ions accelerated to 20 keV was used to excavate shallow pits ranging from 3 to 10 μm across. The primary current was adjusted for each measurement to obtain a count rate of negative ^{16}O ions of ~3.5 to 4×10^5 cps. A normal-incident electron gun was used for charge compensation of the analyzed areas. Negative secondary ions from the ^{16}O tail, ^{16}O, ^{17}O, ^{16}OH, and ^{18}O were analyzed at a mass resolution power of ~6000, sufficient to completely separate hydride interference on ^{17}O. Secondary ions were detected by an electron multiplier in pulse counting mode, and analyses were corrected for dead time. Each analysis is based on 60 cycles collected during 50 min of sputtering time. The detected isotopic ratios are converted to units of $\delta^{17}O$ and $\delta^{18}O$, parts-per-thousand relative to standard mean ocean water (SMOW), using a Russian spinel (SPU) with known O isotopic composition as a standard. From these values, we calculate $\Delta^{17}O = \delta^{17}O - 0.52 \times \delta^{18}O$, which, for our results, describes the extent of ^{16}O-enrichment (or depletion) in the analyzed grains. Typical mass-dependent fractionation leads to changes in $\delta^{17}O$ and $\delta^{18}O$, but $\Delta^{17}O$ remains constant (Clayton et al. 1991; McKeegan and Leshin 2001).

Uncertainties in the SIMS analyses stem from: 1) statistical error based on the number of counts detected; 2) matrix effects between samples and standards; 3) variations in instrumental mass fractionation, which may arise from differences in sample polish, sample topography, beam stability, sputtering rate, condition of the thin conductive layer (for our sample, a carbon coat) on the sample surface, and sample holding (e.g., Shimizu and Hart 1982; Eiler et al. 1997). We estimate statistical error in this study from the standard deviation of the mean of 60 cycles per analysis, generally yielding uncertainties of 2.0 to 2.5 (1σ) in $\delta^{17}O$ and 1.2 to 1.7 (1σ) in $\delta^{18}O$. The matrix effects under the operating conditions used at TiTech have been examined by comparing analytical results for a variety of minerals with known O isotopic composition, including SPU spinel (from Russia), anorthite (Miyake-jima, Japan), augite (Takashima, Japan), and synthetic gehlenite and åkermanite. The reproducibility of $^{17\ or\ 18}O/^{16}O$ on different analysis points from the same standard was ~5‰ (1σ). Matrix effects on detected O isotopic composition among the minerals analyzed are also limited to about 5‰ (Ito et al. 1998). Therefore, we used one standard, the SPU spinel, to determine instrumental mass fractionation during each analytical session.

In addition to the random uncertainties, we suspect that our analyses of phases from the coarse-grained CAI (CGI-10) were affected by a systematic error that displaced results to the ^{18}O-rich side (probably having mass fractionation slope) of the carbonaceous chondrite anhydrous mineral line (CCAM). To evaluate the significance of the discrepancy between the CCAM and most of our results from CGI-10, and to evaluate reproducibility, multiple SIMS analyses were collected over several analytical sessions from one crystal of fassaite in the interior of CGI-10. Seven analyses were collected within a radius of 50 μm, and three other analyses were collected from the same crystal but slightly more distant from the main cluster (Fig. 1a). This approach is based on the assumption that the true fassaite isotopic composition is constant for all sputtered craters. This assumption seems to be appropriate because of our consistent ^{16}O-rich results from other fassaite crystals in CGI-10 and constant isotopic compositions for fassaite determined from multiple in situ analyses in type B CAIs from Allende (Yurimoto et al. 1994; Young and Russell 1998); variable isotopic compositions have been determined for fassaite in some CAIs, but these are from texturally distinct palisade bodies (Kim et al. 2002) and an unusual CAI with ^{16}O-poor and ^{16}O-rich melilite (Yurimoto et al. 1998). Error ellipses showing 95% confidence limits were calculated from the seven closely spaced analyses and from all ten analyses (Fig. 1b). Both error ellipses overlap with the CCAM, indicating that, although most analyses fall to the right of the CCAM, compositions along and on the opposite side of the CCAM are within the 95% confidence limits of repeated analyses of the fassaite. This conclusion is based simply on the distribution of repeated analyses of a mineral with an assumed constant isotopic composition; it does not presume a systematic error.

The results from analytical session B14 suggest that true compositions of melilite from CGI-10 may be closer to the CCAM than indicated by most analytical results (Fig. 2). Charging was suspected for the first analysis of melilite in this session. The sample holder was changed, and analysis B14-2 was collected adjacent to B14-1 and yielded a result closer to the CCAM (Fig. 2b). However, charging was still suspected; thus Al-foil was inserted on the PTS surface to enhance the electrical connection between the PTS and the ground. B14-3 and all subsequent analyses from this session were collected with this geometry. Analysis B14-3 was collected in melilite approximately 25 μm from B14-2 and B14-3 and similar distances from analyses B6-1 and B6-2. B14-3 falls on the CCAM (Fig. 2b). Analyses B14-4 and B14-5 were also collected in melilite adjacent to previously analyzed spots and showed a consistent shift toward the CCAM. The mean compositional displacement of analyses B14-3, 4, and 5 from nearby analyses collected during other analytical sessions is 9‰ down a slope of 0.3 (Fig. 2b). Note, however, that the analyses of ^{16}O-rich minerals collected during this session fall to the right of the CCAM (Fig. 2a). Because of this deviation
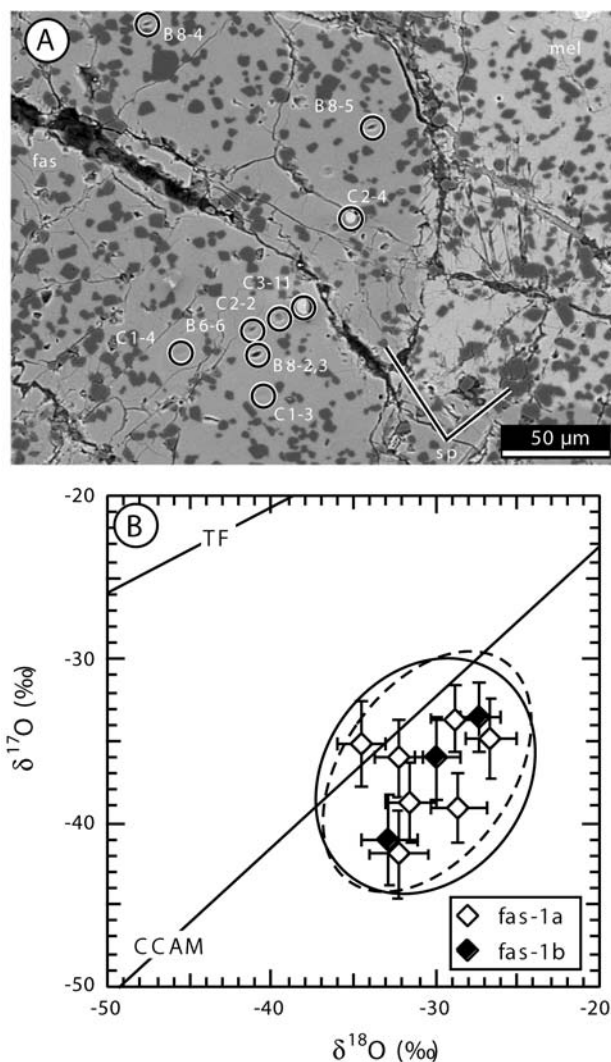

Fig. 1. Reproducibility of SIMS analyses: a) BSE-image showing the locations of multiple SIMS analyses from a single fassaite (fas) crystal in CGI-10. Fas has numerous spinel (sp) inclusions and occurs adjacent to melilite (mel). Six of the analyses are from a small region (radius <50 μm) of the pyroxene and are labeled "fas-1a" in (b). Analyses B08-4, B08-5, and C02-4 are from the same pyroxene crystal, but outside of this small region, and are labeled "fas-1b" in (b); b) oxygen isotopic results from the fassaite crystal. The error ellipse with the solid line encloses the composition of the pyroxene within a 95% certainty level based on the fas-1a analyses. The ellipse with the dashed line is based on all of the analyses. The error bars show ±1σ as the standard deviation of the mean for each analysis. Terrestrial fractionation (TF) and carbonaceous chondrite anhydrous mineral (CCAM) lines are shown for reference.

from the CCAM and to maintain consistent analytical procedure with previously collected results, we reverted to the original holder for sessions after B14. Using Al-foil with the original holder did not cause a shift in detected values.

The shift in oxygen isotopic composition observed for coarse-grained melilite in session B14 suggests that our results from CGI-10 were affected by a systematic error
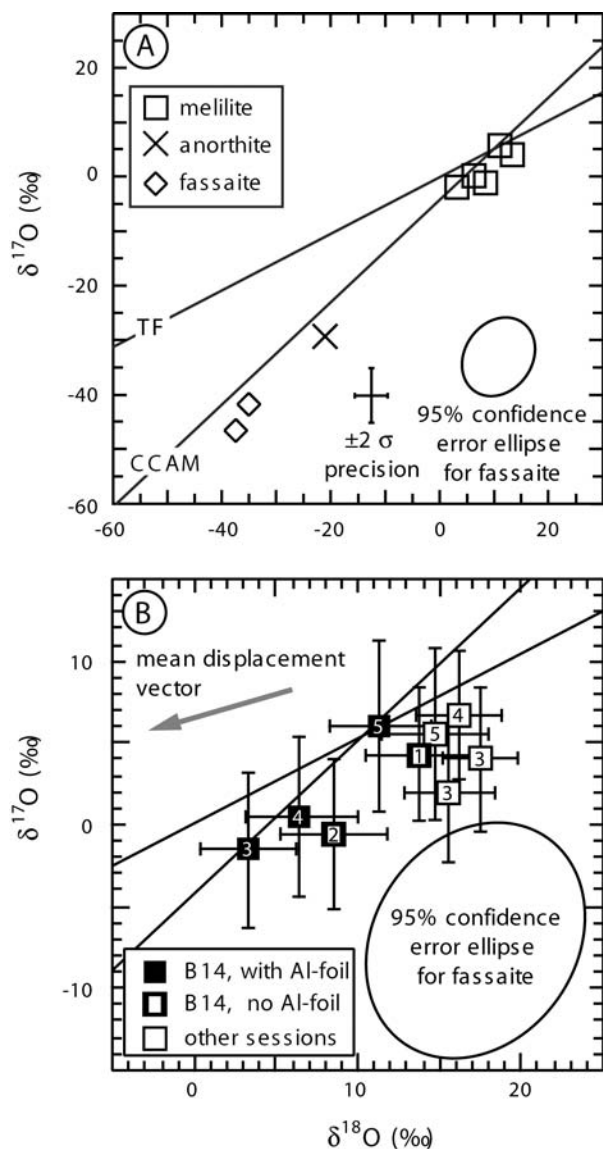
Fig. 2. Results from SIMS session B14 (a) and the comparison of oxygen isotopic analyses of CGI-10 melilite collected during session B14 with analyses from other sessions (b). The numbers correspond to the B14 analyses. Analyses from the other sessions were collected within 40 μm of the corresponding B14 locations. Analysis B14-1 was collected in the same vicinity as B14-3, but the sample holder was changed and Al-foil was placed on the sample surface between the two analyses. The foil was used for all analyses collected in this session after B14-3. Analyses from other sessions include, from top to bottom: B6-3, C3-8, B6-1, and B6-2. Chords were drawn connecting B6-3 with B14-4, C3-8 with B14-5, and the average of B6-1, B6-2, and B14-1 with B14-3. The mean slope and length of these three chords are shown as the "mean displacement vector." The slope of this vector is parallel to the TF line within the error.

parallel to the terrestrial fractionation line (TF), within the uncertainties of statistical errors, as would be expected for a mass-dependent fractionation. This systematic error has a minimal effect on $\Delta^{17}O$. In fact, the three melilite analyses from B14 that fall on the CCAM (B14-3, 4, and 5) have

values of $\Delta^{17}O$ that are within 1σ in analytical precision of the nearby analyses from previous sessions. Furthermore, the systematic error in $\delta^{17}O$ and $\delta^{18}O$ of CGI-10 analyses is much smaller than the differences between ^{16}O-rich and ^{16}O-poor minerals in CAIs. Therefore, even with the systematic error, we are confident that our results from CGI-10 are effective for distinguishing ^{16}O-poor from ^{16}O-rich minerals.

In contrast to the results from CGI-10, SIMS analyses from the fine-grained CAI FGI-12 scatter on both sides of the CCAM (see the Results section). It is possible that the electrical charge introduced by the primary ion beam was dispersed more efficiently in FGI-12 because of the higher concentration of grain boundaries in the fine-grained CAI. If so, then the deviation of the CGI-10 results from the CCAM may have been a consequence of charging at the sample surface.

Areas selected for analyses were imaged in BSE or SE before and after sputtering to verify mineralogy. Most of the sputtered pits are located entirely or nearly so (>90%) in a single type of mineral in the FGI and in a single mineral grain in the CGI. However, in some cases, analysis pits overlap on significant fractions of two or more minerals. In these cases, percentages of sputtered material from different phases were estimated from BSE and SE images. Through an oversight, BSE and SE images were not collected after one analytical session (B16), and the sample surface was repolished. However, the SIMS craters were examined in reflected light before the removal of the carbon coat, and the craters and minerals were well-resolved (all analyses from session B16 were in the CGI). Our estimates of sputtered proportions are on the order of ±5%, although variations in sputtering depth and three-dimensional crystal boundaries may lead to greater errors in some cases in the fine-grained CAI.

RESULTS

Coarse-Grained CAI (CGI-10)

Textures and Mineralogy

CGI-10 is roughly spherical in shape, with a diameter of 4–5 mm, and is dominated by coarse prismatic grains of melilite, Al, Ti-diopside (fassaite), and anorthite, all with multiple inclusions of fine-grained (~5–10 μm across) spinel (Figs. 3 and 4). The mineralogy of this CAI and the coarse-grained texture and melilite-mantle are consistent with a classification as a type B1 CAI (Wark and Lovering 1977). Melilite crystals in the interior of the CAI form elongate euhedral prisms up to 1400 × 200 μm in thin section and exhibit core-to-rim variations from blue to brown birefringence reflecting normal zoning from $\sim Åk_{40}$ to $Åk_{70}$. Melilite in the CAI mantle also forms normally zoned, prismatic crystals, though the crystals are finer grained and the compositions are more gehlenitic ($\sim Åk_{10}$ to $Åk_{50}$). Melilite crystals from both the mantle and interior are essentially gehlenite-åkermanite solid solutions, with Na_2O
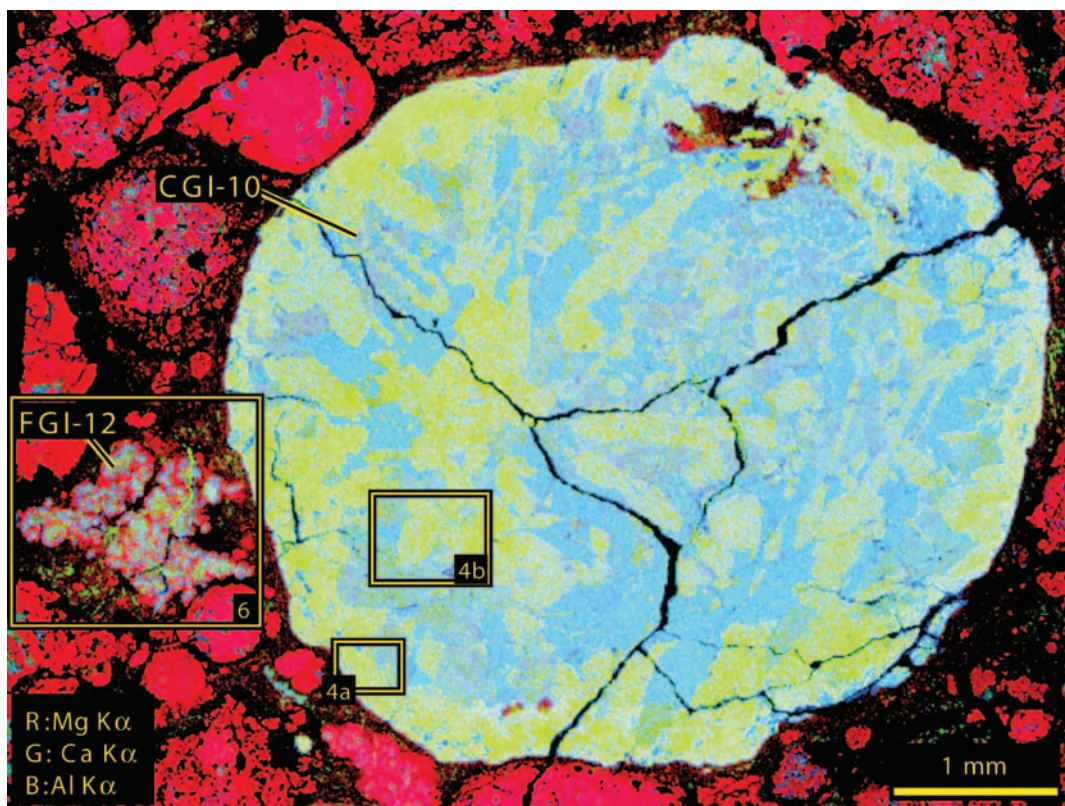
Fig. 3. False-color X-ray elemental map (red = MgKα, green = CaKα, blue = AlKα) of a portion of Efremovka showing coarse-grained CAI CGI-10 and fine-grained CAI FGI-12. In the CAIs, minerals correspond in general to the following color scheme: green = melilite; light blue = anorthite; dark violet = spinel; purple-red = fassaite; bright red = forsterite. The irregular dark red patch near the top of CGI-10 consists of matrix material filling a cavity or embayment in the CAI. Both of the CAIs are cut by weathering veins and fractures. The bright red materials near the CAIs on this image consist mostly of forsterite and enstatite in chondrules and amoeboid olivine aggregates. Matrix silicates have lower Mg/(Mg + Fe) and appear darker red. The yellow boxes show areas shown in greater detail (Figs. 4 and 6).

and FeO concentrations near or below EPMA detection limits (Table 1). Fine equant inclusions of spinel occur in melilite in both mantle and interior domains but are more abundant in melilite from the interior of the CAI (compare Figs. 4a and 4b). Some melilite crystals in the CAI interior exhibit a variation in the concentration of spinel inclusions, with melilite cores having fewer inclusions than melilite rims. Melilite in the CAI mantle also hosts inclusions of perovskite, which occur both as isolated crystals and as aggregates of very fine-grained elongate blebs (Fig. 4a).

Anorthite and fassaite form coarse, subhedral to anhedral crystals in the CAI interior ranging up to about 400 µm long (Figs. 3 and 4b). Anorthite has a nearly pure composition with only minor Na_2O (Table 1). The fassaite also has only minimal Na_2O, and FeO concentrations are near or below EPMA detection limits. Spinel inclusions on the order of 10 µm across are pervasive and abundant in anorthite and fassaite (Fig. 4b).

Oxygen Isotope Analyses

Oxygen isotopic compositions of minerals from CGI-10 fall into two distinct clusters: an ^{16}O-rich cluster consisting of spinel, fassaite, and anorthite and an ^{16}O-poor cluster of

melilite (Table 2; Fig. 5). Results fall along or to the right of the carbonaceous chondrite anhydrous mineral (CCAM) line. Most of the melilite results, in particular, fall well to the right of the CCAM.

As discussed in the Analytical Methods section, we suspect that this deviation from the CCAM is due to a systematic error that caused a mass-dependent fractionation to erroneously high values of $\delta^{17}O$ and $\delta^{18}O$. However, it remains possible that the melilite results reflect true shifts in composition from the CCAM. Oxygen isotopic compositions that fall to the right of the CCAM have been identified in melilite from sodic-altered domains in an Allende CAI and are attributed to mass-dependent fractionation, possibly due to aqueous alteration or rapid melting/evaporation events (Young and Russell 1998). Although it is possible that a similar process affected CGI-10 melilite, no correlation between petrographic evidence of alteration and isotopic composition in CGI-10 has been identified. Also, deviations to the right of the CCAM in many analyses of ^{16}O-rich phases from CGI-10 could be attributed to mass-dependent fractionation effects similar to those inferred for FUN CAIs (Davis et al. 1991). However, multiple analyses collected during several sessions from a small domain in a fassaite crystal indicate that our
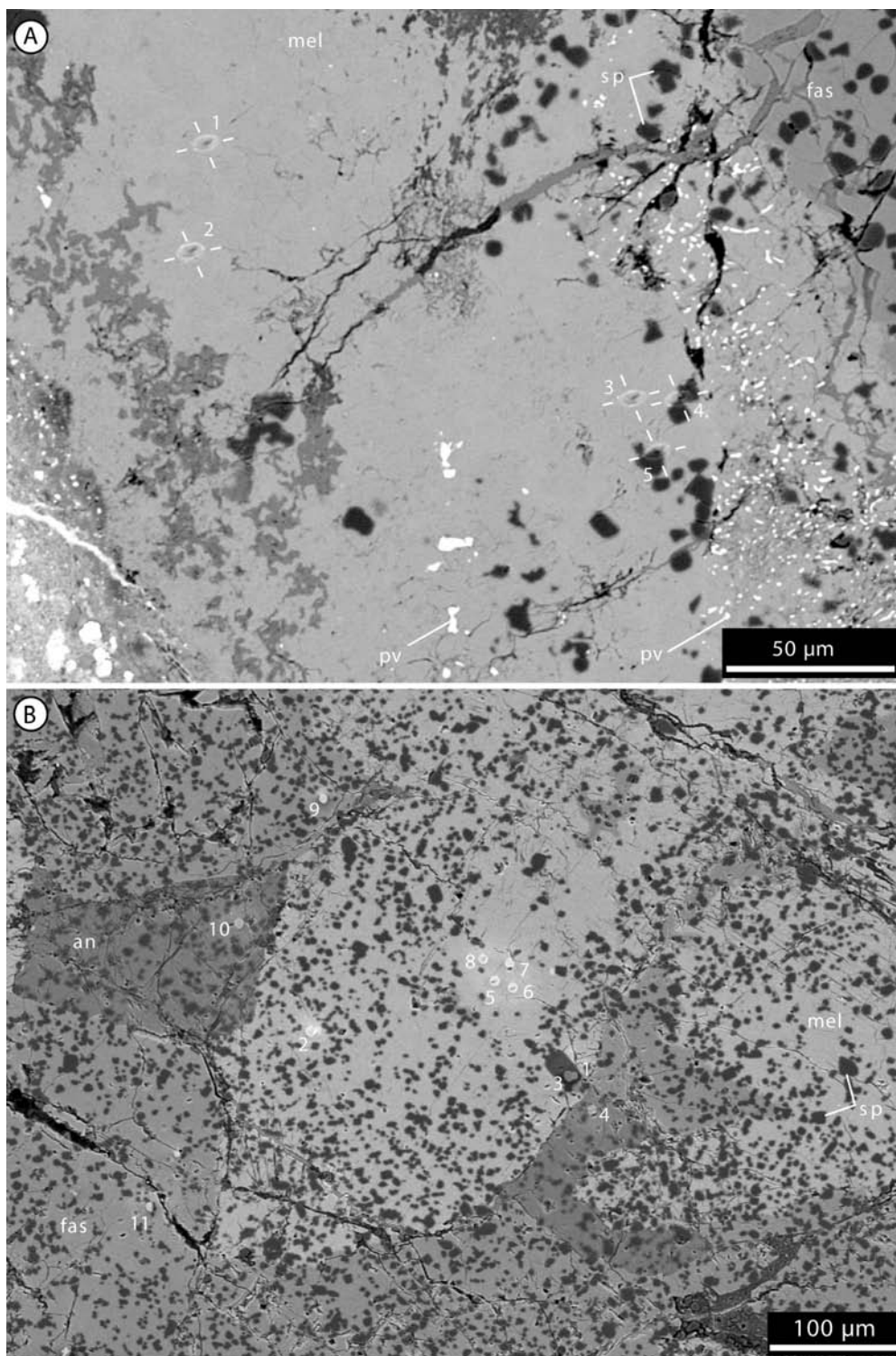
Fig. 4. Backscattered electron (BSE) image from the melilite-rich mantle and composite BSE/secondary electron (SEM) image (a) and from the interior of CGI-10 (b) (Fig. 1): a) craters sputtered during SIMS analyses are highlighted by white dash-marks with numbers corresponding to analyses from session B06 (Table 2). A small portion of the boundary of the CAI with matrix material is shown at the lower left; b) in this composite, a secondary electron image is overlain on a BSE image. The intensities of the two original images are adjusted so that most of the grayscale variations reflect composition (BSE), but the craters sputtered by SIMS analyses, which are bright in the SEM image, are also evident. The bright oval and circular spots are craters sputtered during SIMS session C03, and the numbers correspond to analyses listed in Table 2. The mineral abbreviations, listed from darkest to brightest in grayscale, are as follows: sp = spinel; an = anorthite; fas = fassaite; mel = melilite; pv = perovskite.

Table 1. Representative electron microprobe analyses (wt%) from CGI-10.

Mineral	Spinel	Fassaite	Fassaite	Anorthite	Mantle melilite	Mantle melilite	Interior melilite	Interior melilite
SiO_2	0.21	40.3	39.5	43.6	25.4	32.7	31.7	37.5
TiO_2	0.30	4.77	20.7	0.07	<0.07	<0.07	<0.07	<0.07
Al_2O_3	71.3	19.8	5.27	36.4	31.3	20.4	22.2	12.5
Cr_2O_3	0.29	<0.12	<0.12	<0.12	<0.12	<0.12	<0.12	<0.12
FeO	<0.04	0.04	<0.04	0.06	0.12	<0.04	<0.04	<0.04
MnO	0.04	<0.04	<0.04	<0.04	<0.04	<0.04	<0.04	<0.04
MgO	27.6	9.92	9.15	0.12	2.21	6.28	5.82	9.83
CaO	0.35	24.5	24.6	19.7	39.4	39.6	40.0	39.3
Na_2O	<0.05	<0.05	<0.05	0.10	0.10	0.18	<0.05	0.09
Total	100.1	99.4	99.2	100.0	98.7	99.2	99.7	99.3
Structural formulae								
O	4	6	6	8	7	7	7	7
Si	0.005	1.48	1.45	2.01	1.17	1.49	1.44	1.71
Al	1.99	0.854	0.895	1.98	1.70	1.10	1.19	0.667
Ti	0.005	0.131	0.145	0.002	b.d.[a]	b.d.	b.d.	b.d.
Cr	0.005	b.d.	b.d.	b.d.	b.d.	b.d.	b.d.	b.d.
Fe	b.d.	0.001	0.000	0.002	0.005	0.000	0.000	0.001
Mn	0.001	b.d.	b.d.	b.d.	b.d.	b.d.	b.d.	b.d.
Mg	0.974	0.541	0.501	0.008	0.151	0.427	0.394	0.666
Ca	0.009	0.960	0.966	0.976	1.94	1.94	1.95	1.92
Na	b.d.	b.d.	b.d.	0.009	0.009	0.016	b.d.	0.008
Total	2.99	3.96	3.96	5.00	4.98	4.97	4.97	4.96
Mg/(Mg + Fe), An, Åk	100	100	100	99	15	43	39	67

[a]b.d. = below detection

Table 2. Oxygen isotopic results (‰ relative to SMOW).[a]

Analysis #	Sputtered material (%)	$\delta^{17}O$[b]	$\pm1\sigma\ \delta^{17}O$	$\delta^{18}O$[b]	$\pm1\sigma\ \delta^{18}O$	$\Delta^{17}O$[b]	$\pm1\sigma\ \Delta^{17}O$
Coarse-grained CAI (CGI-10)[c]							
B06-1	mel (100)	3.9	±2.2	17.4	±1.2	−5.1	±2.3
B06-2	mel (100)	1.9	±2.1	15.5	±1.4	−6.2	±2.2
B06-3	mel (100)	6.6	±2.0	16.1	±1.3	−1.8	±2.1
B06-4	spn (55), mel (45)	−15.1	±2.1	−3.7	±1.5	−13.2	±2.2
B06-5	spn (75), mel (25)	−28.1	±2.3	−21.4	±1.5	−17.0	±2.4
B06-6	fas (100)	−33.6	±2.0	−28.8	±1.5	−18.6	±2.1
B06-7	mel (100)	5.8	±1.8	20.1	±1.5	−4.7	±2.0
B07-1	mel (100)	14.0	±2.3	19.0	±1.7	4.1	±2.5
B07-2	spn (100)	−47.1	±2.4	−38.6	±1.5	−27.0	±2.5
B07-3	mel (100)	5.0	±2.7	20.4	±1.5	−5.6	±2.8
B07-4	mel (100)	6.6	±2.1	19.0	±1.6	−3.3	±2.3
B07-5	mel (100)	6.3	±2.2	17.5	±1.2	−2.8	±2.3
B07-6	ano (100)	−37.5	±2.7	−33.2	±1.5	−20.2	±2.8
B07-7	ano (100)	−41.5	±2.5	−32.3	±1.7	−24.7	±2.7
B07-8	fas (60), spn (40)	−44.8	±2.2	−30.8	±1.5	−28.8	±2.3
B07-9	fas (100)	−39.6	±2.6	−31.7	±1.6	−23.1	±2.7
B07-10	fas (100)	−40.3	±2.7	−31.7	±1.3	−23.8	±2.8
B08-1	mel (100)	7.2	±2.3	18.8	±1.6	−2.6	±2.4
B08-2	fas (100)	−41.9	±2.7	−32.3	±1.8	−25.1	±2.9
B08-3	fas (100)	−34.8	±2.4	−26.6	±1.6	−21.0	±2.5
B08-4	fas (100)	−41.0	±2.7	−32.8	±1.7	−23.9	±2.8
B08-5	fas (100)	−36.0	±2.5	−29.9	±1.4	−20.5	±2.6
B08-6	ano (100)	−43.7	±2.3	−33.1	±1.6	−26.5	±2.4
B08-7	mel (100)	6.4	±2.3	17.6	±1.8	−2.8	±2.5
B08-8	mel (100)	−1.9	±2.3	11.0	±1.4	−7.6	±2.4
B14-1	mel (100)	4.2	±2.0	13.6	±1.6	−2.9	±2.2
B14-2	mel (100)	−0.8	±2.3	8.5	±1.6	−5.2	±2.4

Table 2. Oxygen isotopic results (‰ relative to SMOW).[a] *Continued.*

Analysis #	Sputtered material (%)	$\delta^{17}O$[b]	$\pm1\sigma\ \delta^{17}O$	$\delta^{18}O$[b]	$\pm1\sigma\ \delta^{18}O$	$\Delta^{17}O$[b]	$\pm1\sigma\ \Delta^{17}O$
B14-3	mel (100)	−1.6	±2.3	3.3	±1.5	−3.3	±2.4
B14-4	mel (100)	0.4	±2.5	6.4	±1.7	−2.9	±2.7
B14-5	mel (100)	6.0	±2.6	11.3	±1.6	0.1	±2.7
B14-6	fas (100)	−46.6	±2.1	−37.5	±1.3	−27.1	±2.2
B14-7	ano (100)	−29.3	±2.2	−21.2	±1.6	−18.3	±2.4
B14-8	fas (100)	−41.8	±2.2	−35.1	±1.3	−23.5	±2.3
B16-1	fas (100)	−33.4	±2.4	−22.8	±1.5	−21.5	±2.5
B16-2	fas (100)	−38.2	±2.4	−29.5	±1.7	−22.9	±2.6
B16-3	ano (100)	−42.2	±2.3	−31.2	±1.6	−26.0	±2.4
B16-4	ano (100)	−42.6	±2.5	−33.2	±1.7	−25.3	±2.7
B16-5	spn (75), ano (25)	−44.6	±2.2	−36.6	±1.5	−25.6	±2.3
B16-6	ano (100)	−41.8	±2.0	−33.3	±1.6	−24.5	±2.2
B16-7	ano (100)	−31.4	±2.5	−25.9	±1.4	−17.9	±2.6
B16-8	ano (50), spn (50)	−33.7	±2.3	−31.5	±1.2	−17.3	±2.4
B16-9	ano (100)	−30.3	±2.4	−22.6	±1.4	−18.5	±2.5
B16-10	ano (100)	−40.0	±2.5	−34.1	±1.3	−22.3	±2.6
B16-11	ano (100)	−41.4	±2.0	−35.4	±1.6	−23.0	±2.2
B16-12	ano (100)	−39.0	±2.0	−29.2	±1.4	−23.8	±2.1
B16-13	mel (100)	5.3	±2.4	9.7	±1.7	0.3	±2.6
B17-1	mel (100)	1.0	±2.4	15.6	±1.9	−7.1	±2.6
B17-2	mel (100)	1.5	±2.5	12.6	±1.8	−5.1	±2.7
B17-3	fas (100)	−36.7	±2.3	−25.4	±1.6	−23.5	±2.4
B17-4	ano (100)	−41.9	±2.1	−34.2	±1.5	−24.1	±2.2
B17-5	fas (100)	−36.4	±2.8	−33.8	±1.3	−18.8	±2.9
B17-6	ano (100)	−43.7	±2.4	−35.2	±1.5	−25.4	±2.5
B17-7	mel (100)	5.6	±2.3	20.5	±1.6	−5.1	±2.4
C01-01	mel (100)	6.0	±2.3	16.7	±1.6	−2.7	±2.4
C01-02	spn (80), mel (20)	−21.0	±2.2	−12.4	±1.5	−14.6	±2.3
C01-03	fas (100)	−35.1	±2.6	−34.5	±1.4	−17.2	±2.7
C01-04	fas (100)	−38.7	±2.4	−31.5	±1.5	−22.3	±2.5
C01-05	ano (100)	−31.8	±2.4	−27.2	±1.2	−17.7	±2.5
C01-06	ano (100)	−37.0	±2.2	−34.8	±1.3	−18.9	±2.3
C01-07	fas (100)	−40.3	±2.4	−29.9	±1.4	−24.8	±2.5
C02-01	fas (75), spn (25)	−32.8	±2.2	−29.7	±1.4	−17.4	±2.3
C02-02	fas (100)	−39.1	±2.1	−28.6	±1.7	−24.2	±2.3
C02-03	mel (100)	10.7	±2.6	21.6	±1.3	−0.5	±2.7
C02-04	fas (100)	−33.5	±2.2	−27.3	±1.2	−19.3	±2.3
C03-01	spn (100)	−41.4	±2.5	−40.5	±1.1	−20.3	±2.6
C03-02	mel (100)	10.5	±2.5	18.0	±1.5	1.1	±2.6
C03-03	spn (100)	−39.9	±2.1	−36.7	±1.3	−20.8	±2.2
C03-04	ano (100)	−37.0	±2.0	−33.4	±1.7	−19.6	±2.2
C03-05	mel (100)	10.5	±1.7	16.3	±1.6	2.0	±1.9
C03-06	mel (100)	12.6	±2.3	19.1	±1.3	2.7	±2.4
C03-07	mel (100)	10.4	±1.9	17.8	±1.3	1.1	±2.0
C03-08	mel (100)	5.4	±2.6	14.6	±1.6	−2.2	±2.7
C03-09	fas (100)	−39.7	±2.5	−29.4	±1.6	−24.4	±2.6
C03-10	ano (100)	−42.4	±2.5	−34.7	±1.2	−24.4	±2.6
C03-11	fas (100)	−36.0	±2.4	−32.2	±1.5	−19.3	±2.5
Fine-grained CAI (FGI-12)							
A01-1	Aldi (60), mel (40)	−22.1	±2.4	−19.7	±1.5	−11.9	±2.5
A01-2	spn (100)	−46.2	±2.4	−48.3	±1.5	−21.1	±2.5
A01-3	mel (95), spn (5)	−11.0	±2.6	−4.1	±1.3	−8.9	±2.7
A01-4	mel (100)	−27.3	±2.5	−27.6	±1.4	−12.9	±2.6
A01-5	mel (100)	−16.0	±2.6	−13.7	±1.5	−8.9	±2.7
A01-6	spn (100)	−47.9	±2.4	−48.2	±1.3	−22.8	±2.5
A01-7	Aldi (80), mtx (15), olv (5)	−27.6	±2.7	−31.2	±1.5	−11.4	±2.8

Table 2. Oxygen isotopic results (‰ relative to SMOW).[a] *Continued.*

Analysis #	Sputtered material (%)	$\delta^{17}O$[b]	$\pm 1\sigma\ \delta^{17}O$	$\delta^{18}O$[b]	$\pm 1\sigma\ \delta^{18}O$	$\Delta^{17}O$[b]	$\pm 1\sigma\ \Delta^{17}O$
A01-8	spn (100)	−43.7	±2.8	−48.0	±1.5	−18.7	±2.9
A01-9	olv (70), Al-di (20), mtx (10)	−32.8	±2.9	−29.4	±1.5	−17.5	±3.0
A01-10	olv (90), Al-di (10)	−42.3	±2.3	−38.4	±1.6	−22.3	±2.4
B08-9	mel (100)	−18.3	±2.7	−14.3	±1.9	−10.9	±2.9
B15-1	spn (100)	−31.2	±2.0	−33.9	±1.6	−13.6	±2.2
B15-2	spn (100)	−43.7	±2.3	−41.8	±1.3	−22.0	±2.4
B15-3	spn (95), pv (5)	−46.0	±1.8	−44.4	±1.3	−22.9	±1.9
B15-4	spn (100)	−49.8	±2.1	−45.7	±1.5	−26.0	±2.2
B15-5	spn (100)	−37.0	±2.7	−32.5	±1.4	−20.1	±2.8
B15-6	mel (95), spn (5)	−42.7	±2.4	−40.0	±1.6	−21.9	±2.5
B15-7	spn (100)	−50.8	±2.4	−42.0	±1.7	−29.0	±2.6
B15-8	Aldi (100)	−38.8	±2.1	−40.2	±1.5	−17.9	±2.2
B15-9	Aldi (100)	−35.1	±2.5	−33.0	±1.4	−17.9	±2.6
B15-10	spn (100)	−45.3	±2.2	−44.6	±1.8	−22.1	±2.4
B15-11	mel (99), spn (1)	−30.0	±2.7	−28.6	±1.5	−15.1	±2.8
B15-12	Aldi (99), mel (1)	−39.4	±2.2	−33.8	±1.6	−21.8	±2.4

[a]Aldi = Al-diopside; ano = anorthite; fas= fassaite; fo = forsterite; mel = melilite; mtx = matrix; olv = olivine; spn = spinel.

[b]σ is calculated as a standard deviation of the mean for 60 cycles per analysis. The estimate of session-to-session reproducibility is shown in Fig. 1.

[c]Analyses from CGI-10 may have been affected by a systematic error that increased values of $\delta^{17}O$ and $\delta^{18}O$, but had only a minor effect on $\Delta^{17}O$. See the Analytical Methods section and Fig. 2.
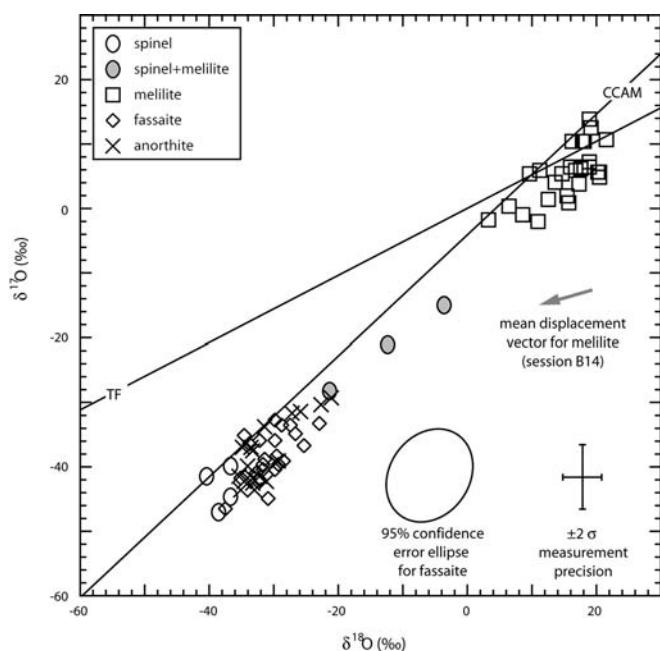

Fig. 5. Oxygen isotopic compositions of minerals analyzed by ion microprobe from Efremovka CGI-10 (Table 2). Results are normalized to standard mean ocean water (SMOW). The error ellipse for fassaite is from Fig. 1. The approximate error bars are shown at right. Reference lines: TF = terrestrial fractionation; CCAM = carbonaceous chondrite anhydrous minerals (Clayton 1993).

estimate of the fassaite composition lies within the analytical uncertainty of the CCAM, even if we assume there was no systematic error in the analyses (see the Analytical Methods section and Fig. 1). Given the uncertainties in our results, it is plausible that the true isotopic compositions of CGI-10 phases are not significantly displaced from the CCAM. In spite of the

uncertainty regarding proximity to the CCAM, all of the melilite analyses we collected from CGI-10 are ^{16}O-poor, and all analyses of spinel, anorthite, and fassaite are ^{16}O-rich. The 95% confidence ellipses from repeated analyses of Al, Ti-diopside and the mean displacement vector showing error related to local charging effects in melilite are small relative to the consistent difference between the ^{16}O-poor and ^{16}O-rich minerals (Fig. 5). Thus, the ^{16}O-rich and ^{16}O-poor clusters of composition shown in Fig. 5 reflect true differences in isotopic composition of minerals from CGI-10. Isotopic analyses were collected from melilite crystals with a range of Åk-contents from the mantle and interior of the CAI, and analyses of spinel, anorthite, and fassaite were collected from the interior and mantle or near-mantle domains. Thus, the isotopic differences in composition correlate directly with mineral type and are insensitive to position in the CAI. The ^{16}O-rich compositions of spinel and fassaite and ^{16}O-poor composition of melilite conform with the pattern observed in many coarse-grained CAIs from Allende. However, in CGI-10, anorthite is ^{16}O-rich, in contrast to the ^{16}O-poor anorthite identified in many Allende CAIs (Clayton et al. 1977; Mayeda et al. 1986; Yurimoto et al. 1994).

Fine-Grained CAI (FGI-12)

Textures and Mineralogy

The fine-grained CAI FGI-12 consists of two objects separated by a thin seam of matrix and is located adjacent to CGI-10 in Efremovka (Figs. 3 and 6). Each object is on the order of 1000 μm in length and is characterized by a highly irregular surface and shape, in contrast to the spherical form and smooth surface of CGI-10. The texture of FGI-12 is dominated by fine-grained, spinel-cored nodules connected
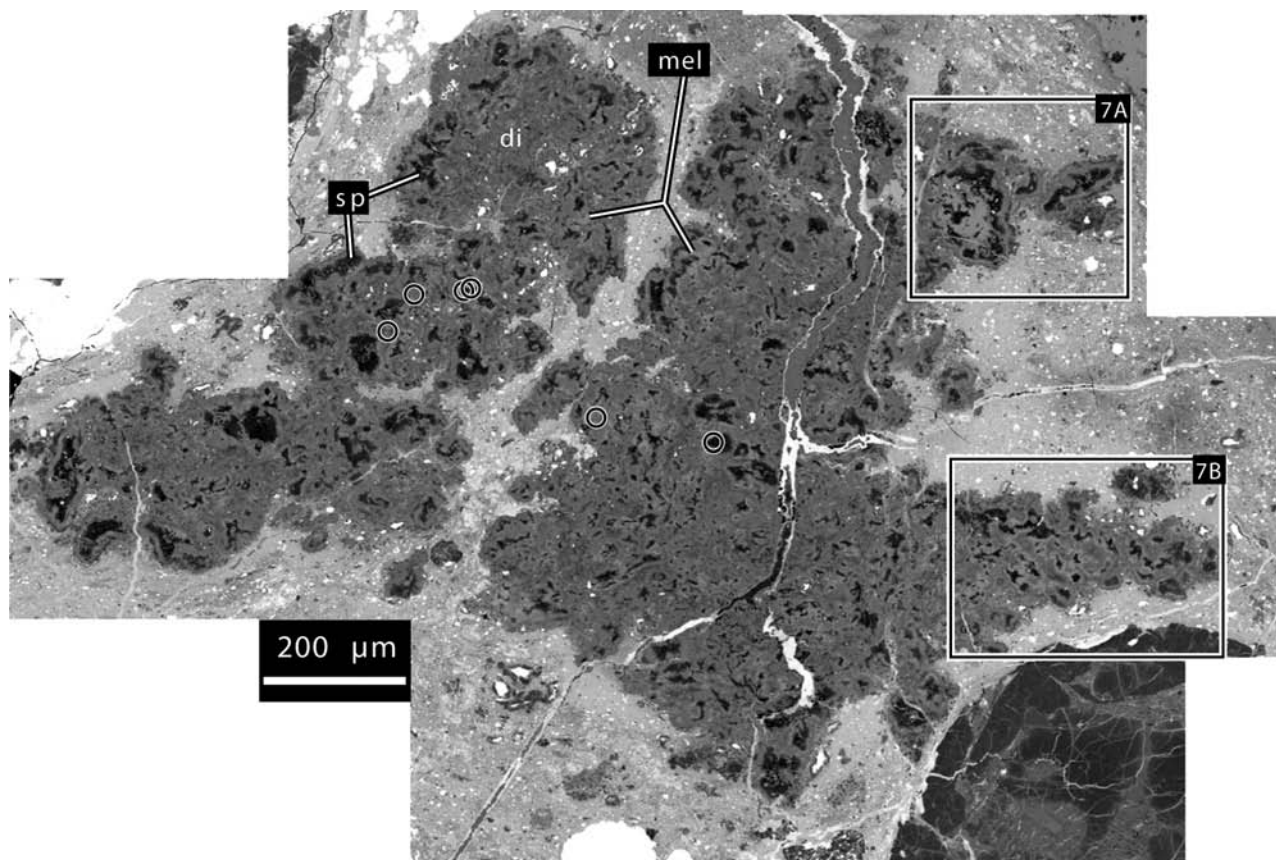
Fig. 6. BSE mosaic of fine-grained CAI Efremovka FGI-12. The areas highlighted in boxes are shown in greater detail in Fig. 7. The circles show the locations of analyses outside of the boxed areas and from left to right are the following analyses from session B15: 9, 12, 10, 11, 8, and 7 (Table 2). Melilite (mel) occurs for the most part as thin layers, relatively bright in BSE, surrounding spinel (sp). The intermediate grayscale area composing most of the FGI consists of fine-grained diopside with variable Al-content (di). The white grains in this image consist mostly of Fe, Ni-metal but also include some fine perovskite.

by fine-grained diopside with variable Al contents (Figs. 6 and 7b; Table 3). The grain sizes of the spinel, melilite, and Al-diopside are difficult to estimate because they are thinner than the thin section and occur in monomineralic aggregates, but most grains are certainly less then 5 μm across and are probably on the order of 1 μm or so in diameter. Grains of Fe, Ni-metal are rare. The nodules consist of a core of fine-grained spinel, which is frequently surrounded by a thin layer of fine-grained melilite ± perovskite (Fig. 7). The spinel cores are typically irregular in outline, as opposed to having simple geometric shapes. Spinel compositions are near the $MgAl_2O_4$ end member but with detectable V_2O_3 and some variations in $MgO/(MgO + FeO)$ (Table 3). Spinel with relatively low $MgO/(MgO + FeO)$ is manifest by lighter grayscale in BSE images and tends to occur close to margins of the FGI (Fig. 7b). The Al-diopside forms an irregular mass of fine grains between the nodules and forms most of the perimeter of the FGI. Forsteritic olivine occurs along the outer margin of a limited portion of the FGI (Fig. 7a; Table 3).

Oxygen Isotope Analyses

Similar to the CGI-10 pattern, spinel and Al-diopside in FGI-12 are ^{16}O-rich ($\delta^{17, 18}O <-30‰$, $\Delta^{17}O <-14‰$), and melilite exhibits a trend toward more ^{16}O-poor compositions (Table 2; Fig. 8). Olivine in FGI-12 is ^{16}O-rich. Mixed analyses of olivine + matrix (A1-9), Al-diopside + matrix (A1-7), and Al-diopside + melilite (A1-1) are shifted toward compositions that are more ^{16}O-poor than analyses of pure Al-diopside and olivine (Table 2; Fig. 8), which is consistent with sputtering of mixtures of ^{16}O-poor and ^{16}O-rich phases. The FGI-12 results fall along the CCAM, in contrast to the results from CGI-10. One pair of analyses collected during different sessions from adjacent spots in melilite in FGI-12 show excellent agreement (A01-5 and B08-9) (Table 2; Fig. 8), indicating that analyses from different analytical sessions produced consistent, comparable results.

Unlike the CGI-10 melilite, melilite from FGI-12 exhibits a gradational shift toward ^{16}O-poor compositions, and isotopic compositions vary from location to location in the fine-grained CAI. No systematic correlation between melilite isotopic composition and proximity to the CAI margin was identified. The spread in isotopic composition in one spinel-cored nodule ranges over 20 to 30‰ over a distance as small as 40 μm (Fig. 7a). The spread in isotopic

Table 3. Representative elemental analyses (wt%) from FGI-12.

Mineral	Spinel	Spinel	Olivine	Al-diopside	Al-diopside	Melilite	Melilite	Melilite
Analysis	wds	wds	eds	eds	eds	eds	eds	eds
SiO_2	0.49	0.28	41.43	49.09	53.04	24.6	27.13	24.12
TiO_2	0.26	0.09	<0.2	0.39	<0.2	<0.2	0.53	<0.2
Al_2O_3	69.36	71.47	0.57[a]	11.22	3.47	31.3	29.47	34.03
V_2O_3	0.67	0.58	<0.2	<0.2	<0.2	<0.2	<0.2	<0.2
Cr_2O_3	0.24	0.09	<0.35	<0.35	<0.35	<0.35	<0.35	<0.35
FeO	5.28	1.21	4.82	0.84	0.58	<0.45	0.54	<0.45
MnO	0.07	<0.04	<0.4	<0.4	<0.4	<0.4	<0.4	<0.4
MgO	24.71	27.79	51.71	14.91	18.02	2.15	3.75	1.74
CaO	0.14	0.2	<0.2	25.55	25.14	41.63	39.91	42.31
Total	101.2	101.7	98.5	102.0	100.3	99.7	101.3	102.2
Structural formulae								
O	4	4	4	6	6	7	7	7
Si	0.012	0.007	0.999	1.74	1.91	1.13	1.22	1.08
Al	1.96	1.98	0.016[a]	0.469	0.147	1.69	1.56	1.79
Ti	0.005	0.002	b.d.[b]	0.01	b.d.	b.d.	0.018	b.d.
V	0.013	0.011	b.d.	b.d.	b.d.	b.d.	b.d.	b.d.
Cr	0.005	0.002	b.d.	b.d.	b.d.	b.d.	b.d.	b.d.
Fe	0.106	0.024	0.097	0.025	0.017	b.d.	0.02	b.d.
Mn	0.001	b.d.	b.d.	b.d.	b.d.	b.d.	b.d.	b.d.
Mg	0.885	0.972	1.859	0.788	0.966	0.147	0.251	0.116
Ca	0.004	0.005	b.d.	0.971	0.969	2.05	1.92	2.02
Total	2.99	3.00	2.97	4.01	4.01	5.02	4.99	5.00
Mg/(Mg + Fe), Åk	89	98	95	97	98	15	25	12

[a]High Al_2O_3 may be due to beam overlap with adjacent matrix phases.
[b]b.d. = below detection.

compositions detected in this nodule may reflect an isotopic gradient on the scale of the nodule, or it may reflect more random alteration patches. If the latter case applies, then gradients in isotopic composition are even steeper than suggested above. In either case, the isotopic gradients preserved in melilite from FGI-12 contrast with the more uniform isotopic compositions detected in CGI-10 melilite.

DISCUSSION

Initial Formation of CGI-10 and FGI-12: Implications for Fine- and Coarse-Grained CAIs

Constraints from Textures and Elemental Compositions.

Spinel, perovskite, Ca-rich pyroxene, and melilite are common to both CGI-10 and FGI-12 and indicate stability in a temperature range of about 1700 to 1300 K, depending on pressure and dust:gas (Grossman 1972; Petaev and Wood 1998; Ebel and Grossman 2000). Anorthite, which is less refractory than diopside, occurs in CGI-10 but not FGI-12. Olivine occurs only in one restricted portion along the external margin of FGI-12, suggesting that most of the initial formation of FGI-12 occurred above olivine condensation temperatures. The primary minerals in FGI-12 and CGI-10 show no textural evidence of extensive recrystallization to hydrous or alkalic or FeO-rich phases similar to those observed in CAIs from Allende (Meeker et al. 1983) and

metamorphosed CO chondrites (Russell et al. 1998). Thus, the mineralogy and textures of FGI-12 and CGI-10 can be attributed mostly to high temperature petrogenesis, $> \sim 1200$ K for CGI-10 and $> \sim 1250$ K for FGI-12 (based on the condensation temperatures of anorthite and olivine, respectively, at 10^{-6} atm; see Ebel and Grossman 2000).

In spite of the similarities in refractory mineralogy, it is clear from differences in texture and mineral composition that CGI-10 and FGI-12 did not form under identical conditions. The euhedral crystal form and normal elemental zoning suggest that melilite in CGI-10 crystallized from a liquid. The variation from more gehlenite-rich compositions of melilite in the CGI mantle to more åkermanitic compositions in the CGI interior can be explained as a result of earlier crystallization of the mantle (MacPherson and Grossman 1981). This inference is supported by the higher concentration of spinel inclusions in melilite from the CGI interior because trapping of inclusions is likely to be more prevalent at later stages of crystallization, when liquid is less free to flow around growing crystal faces. The presence of euhedral spinel inclusions in the other major phases of CGI-10 indicates that spinel crystallized relatively early, while the occurrence of fassaite and anorthite in the interior of the CAI and the subhedral to anhedral textures of these minerals indicate that fassaite and anorthite mostly post-dated melilite crystallization. This timing sequence fits phase relationships for systems with CAI-like compositions (Stolper 1982).
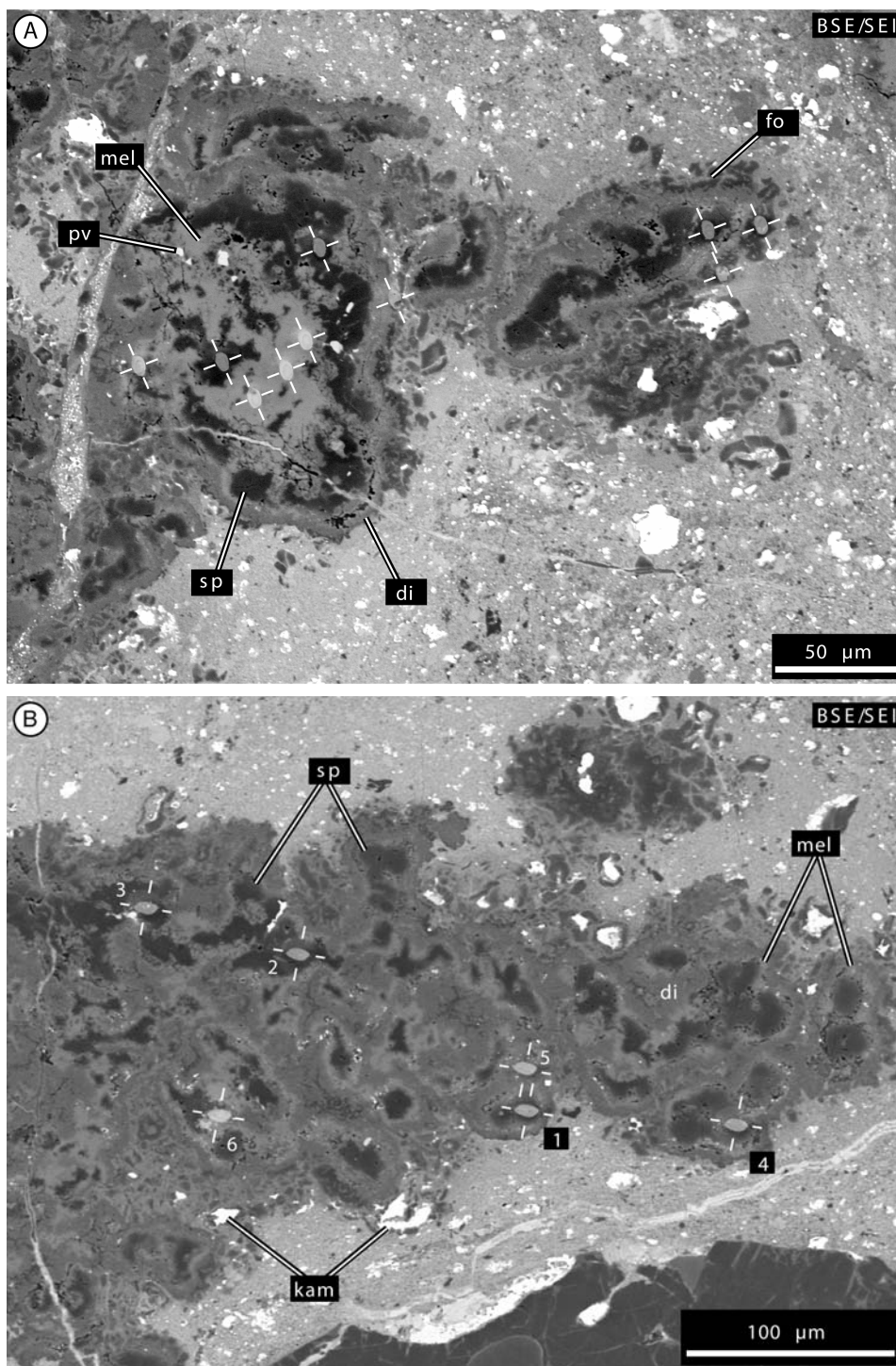
Fig. 7. Composite BSE/SEM overlays showing textures and locations of isotopic analyses from FGI-12 (Fig. 6). Most of the grayscale contrast is controlled by BSE, but craters sputtered during SIMS analyses are dominated by SE contrast. Craters sputtered during isotopic analyses are highlighted by white dash-marks: a) melilite-rich portion of FGI-12 (Fig. 4). The nodular texture is similar to the rest of the FGI, but the melilite layer around spinel is relatively wide. The melilite is composed of many fine grains on the order of 1 μm in diameter. Forsterite (fo) rims a portion of the FGI in this region. The other mineral abbreviations are the same as in previous figures. SIMS craters were in sputtered session A1 and from left to right are analyses: 1, 2, 3, 5, 4, 6, 7 (poor SE contrast of this crater), 8, 9 and 10 (Table 2); b) the nodular texture is typical of most of FGI-12. The nodules have spinel (sp) cores and thin melilite (mel) mantles and are connected by a very fine-grained mass of diopside (di) with variable Al-contents. The relatively coarse, bright grains are Fe, Ni-metal (kam), but many of the very fine bright grains appear to be perovskite. SIMS craters were sputtered in session B15 and from left to right are analyses: 3, 6, 2, 1 (close to FGI margin), 5 (above 1), and 4 (Table 2).
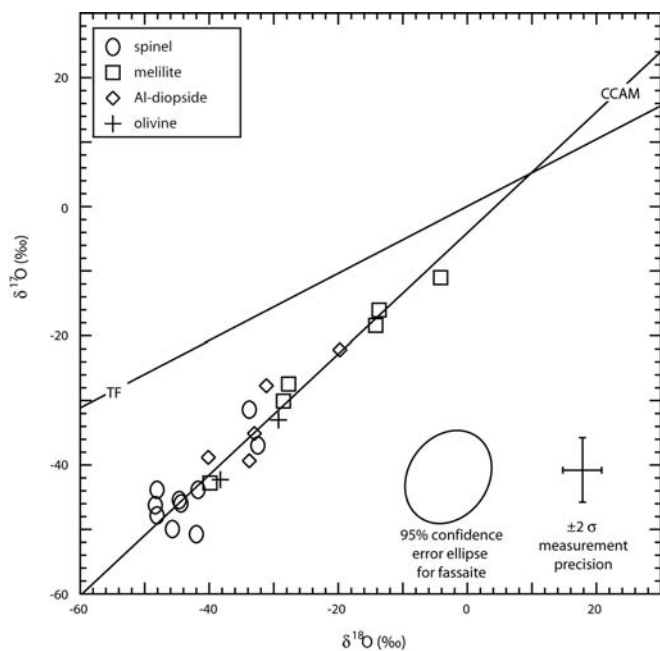
Fig. 8. Oxygen isotopic compositions of minerals analyzed by ion microprobe from Efremovka FGI-12 (Table 2).

Furthermore, the near-circular cross section of CGI-10 in thin section and the consistent core-to-mantle variations in mineralogy suggest that CGI-10 crystallized as a single entity from one drop of liquid.

In contrast, FGI-12 has a more complex external margin and appears to have grown by coalescence of multiple spinel-cored nodules (Fig. 6). The spinel occurs as very fine grains in mono-mineralic aggregates with contorted shapes (Fig. 7) indicating that the aggregates either quenched from deformed liquid droplets or coalesced from previously existing spinel grains. The differences in MgO/(MgO + FeO) of spinel (Table 3) probably result from variable effects of secondary alteration after the CAI formed. This is consistent with the occurrence of FeO-rich spinel near margins of the CAI. Variations in spinel MgO/(MgO + FeO) can also be produced during condensation as a result of differences in pressure and the dust/gas ratio, but FeO-enrichment in this setting should be accompanied by major substitution of Cr for Al (Ebel and Grossman 2000), which is not observed in the FGI-12 spinel. Melilite and Al-diopside in FGI-12 are also very fine-grained, and although variations in composition occur (Table 3), no igneous zoning profiles comparable to those identified in CGI-10 melilite have been identified.

Mineral textures and compositions indicate that the spinel-cored nodules may have formed as independent condensation sequences. However, the nodule textures suggest that spinel cores formed before melilite mantles, and this is opposite to the expectation from equilibrium condensation models, as melilite condenses at higher temperatures than spinel (Grossman 1972; Petaev and Wood

1998; Ebel and Grossman 2000). As pointed out by MacPherson et al. (2002), this conflict between textures and equilibrium condensation temperatures is a long-standing issue. As an alternative to direct condensation, Kornacki and Wood (1985) inferred that fine-grained spinel-rich inclusions underwent melting and distillation caused by gas drag. Yet, the textures in FGI-12 and similar fine-grained refractory inclusions are not suggestive of crystal growth in a liquid. Thus, the detailed petrogenesis of FGI-12 remains elusive.

Oxygen Isotopes

Results from natural CAIs (Clayton 1993; Young and Russell 1998; Yurimoto et al. 1998; Wasson et al. 2001) and diffusion experiments (Yurimoto et al. 1989; Ryerson and McKeegan 1994; Ingrin et al. 2001) show that spinel, diopside, and anorthite are more resistant to exchange of oxygen isotopes than melilite. Thus, the ^{16}O-rich composition of these phases in CGI-10 and FGI-12 indicate that both of these CAIs initially formed under ^{16}O-rich conditions, similar to many refractory inclusions found in chondrites. The association of ^{16}O-rich compositions with refractory inclusions was discovered from bulk analyses of mineral separates, dominantly from the oxidized CV3 Allende (Clayton et al. 1973, 1977) and subsequently from the CM2 Murchison (Clayton and Mayeda 1984). With the development of secondary ion microscopy, ^{16}O-rich CAIs have also been identified in reduced CV3 (Krot et al. 2002), CR (Aléon et al. 2002), CO (Wasson et al. 2001), CH (Sahijpal et al. 1999), ordinary (McKeegan et al. 1998), and enstatite (Guan et al. 2000; Fagan et al. 2001) chondrites and in the unclassified carbonaceous chondrite Acfer 094 (Fagan et al. 2003). However, not all refractory materials are ^{16}O-rich. CAIs with ^{16}O-poor compositions have been identified in the CH (Sahijpal et al. 1999) and EL (Fagan et al. 2001) chondrites, and CAIs in two metal-rich chondrites in the CR clan have intermediate compositions ($\delta^{17, 18}O \sim -10$ to $-20‰$; Krot et al. 2001). Despite these exceptions, most refractory inclusions, including CGI-10 and FGI-12 of this study, are associated with ^{16}O-rich compositions. In competing models, the ^{16}O-rich component has been attributed to: 1) a nucleosynthetic source (Clayton et al. 1973; Clayton 1993); 2) non-mass-dependent fractionation of gaseous species (Thiemens and Heidenreich 1983; Thiemens 1999); and 3) photochemical self-shielding (Clayton 2002, 2004; Lyons and Young 2004).

O-Isotopic Exchange in Melilite from CGI-10 and FGI-12

Fine-grained melilite from FGI-12 is variably depleted in ^{16}O, while coarse-grained melilite from CGI-10 has undergone complete isotopic re-equilibration with an ^{16}O-poor reservoir. This contrast in alteration pattern is opposite to the contrast predicted by a parent body alteration model in which fine-grained melilite should be altered completely before complete

alteration of coarse-grained melilite. Therefore, the two CAIs must have undergone isotopic exchange under different physical conditions. Partial isotopic exchange in melilite in FGI-12 may have occurred during or before parent body metasomatism. The more complete isotopic alteration of coarse-grained melilite in CGI-10 required a more extreme set of conditions, probably greater duration, temperature, or isotopic gradient, than the event that affected FGI-12. If the CGI-10 alteration event had occurred while the two CAIs were adjacent to each other on the Efremovka parent body, this event would have resulted in complete alteration of the finer grained melilite in FGI-12. Therefore, depletion of ^{16}O in the CGI-10 melilite must have preceded incorporation of CGI-10 in the Efremovka parent body. Furthermore, the ^{16}O-rich composition of anorthite in CGI-10 indicates that O isotopic exchange in melilite in this CAI occurred without any similar effects in coexisting anorthite.

To interpret the variable isotopic results from melilite in FGI-12, the roles of diffusion and dissolution/ reprecipitation must be considered. Melilite in FGI-12 might have altered its O isotopic composition by diffusion with a ^{16}O-poor reservoir, possibly an aqueous fluid. If so, variations in isotopic composition might have resulted from original variations in grain size, with finer grains more completely altered than coarser grains. In this case, ^{16}O-poor melilite could have been produced by either of two mechanisms: 1) diffusion of oxygen from fluid into adjacent pre-existing grains; or 2) dissolution and reprecipitation (Wasson et al. 2001; Imai and Yurimoto 2003; Fagan et al. 2004). Both of these mechanisms would produce more ^{16}O-poor melilite in domains that experienced greater fluxes of fluid. A diffusion-controlled mechanism would be expected to produce smooth gradients in isotopic composition within grains, while a dissolution/reprecipitation mechanism could produce discontinuities in composition at boundaries between original and reprecipitated melilite; however, melilite grain sizes in FGI-12 are too fine to detect any possible within-grain discontinuities. Three analyses from a melilite-rich region of FGI-12 form a simple linear trend of isotopic composition with distance (Table 2; Fig. 7a), supporting a gradient produced by a variation in flux of ^{16}O-poor fluid. However, these are only three analyses, and a more detailed study of the distribution of oxygen isotopes is required to interpret the variations in isotopic composition in melilite from FGI-12.

Melilite in CGI-10 is very coarse-grained and must have been altered by diffusion through bulk material instead of along grain boundaries. However, it is not clear whether or not the bulk diffusion was through a solid melilite crystal lattice. Oxygen diffuses more rapidly in melilite than in the other major phases of CGI-10, but quantitative modeling indicates that the oxygen isotopic distribution in coarse-grained CAIs is probably not a consequence of variable diffusion rates in melilite, diopside, anorthite, and spinel

(Yurimoto et al. 1991; Ryerson and McKeegan 1994). The Yurimoto et al. (1991) and Ryerson and McKeegan (1994) studies attempted to model a typical Allende pattern of O isotopic distribution (i.e., with ^{16}O-rich spinel, slightly ^{16}O-depleted diopside, extensively ^{16}O-depleted anorthite, and the most ^{16}O-poor compositions in melilite; see Clayton 1993; Yurimoto et al. 1994). This pattern is different from the CGI-10 pattern, in which anorthite is ^{16}O-rich. However, this difference does not resolve the difficulties of modeling the O isotopic distribution of CGI-10 as a consequence of variable diffusion rates. In fact, in isothermal models, preserving ^{16}O-rich anorthite during complete isotopic exchange in melilite does not appear to be possible under any of the temperature-time combinations in either of the Yurimoto et al. (1991) or Ryerson and McKeegan (1994) studies.

Furthermore, isotopic exchange by lattice diffusion in melilite is contradicted by sharp boundaries in isotopic composition within single crystals of melilite in CAIs from Allende (Yurimoto et al. 1998) and Vigarano (Harazono and Yurimoto 2003). Diffusion, particularly during late stages of re-equilibration, tends to produce smooth compositional gradients. The presence of sharp boundaries in oxygen isotopic composition within single crystals of melilite favors some kind of discontinuity in isotopic exchange, which conflicts with the continuous compositional gradients produced by simple diffusion. This inference is in agreement with the observation that coarse-grained fassaite, spinel, and anorthite in an Allende CAIs have homogeneous isotopic compositions without detectable gradients in composition near cracks or grain margins (Yurimoto et al. 1994).

It has been proposed that rapid heating and cooling of CAIs in the presence of an ^{16}O-poor gas led to disequilibrium melting of melilite, while other phases remained solid, and that rapid diffusion in melilite liquid resulted in the ^{16}O-poor melilites characteristic of coarse-grained CAIs (Yurimoto et al. 1998). Under this scenario, it is possible that some melilite domains did not melt and retained their ^{16}O-rich compositions (Harazono and Yurimoto 2003). This model is supported by experimental evidence that melting of melilite is kinetically favored in comparison to melting of other typical CAI phases (Greenwood and Hess 1996; Greenwood 2004). Isotopic exchange between ^{16}O-poor gas and silicate liquid is consistent with the observation that igneous textures in CAIs from CR chondrites are associated with ^{16}O-depleted compositions (Aléon et al. 2002). The rapid heating and cooling required by this model indicate a nebular setting for isotopic alteration of CAIs because diffusion of heat in a parent body would dampen rates of heating and cooling. A nebular setting is consistent with this study, which shows that isotopic exchange in melilite in CGI-10 and, by inference, similar coarse-grained CAIs in carbonaceous chondrites occurred before parent body processing.

CONCLUSIONS

Comparison of the distribution of oxygen isotopes in two adjacent CAIs from Efremovka—one fine-grained and the other coarse-grained—indicates that the two CAIs: 1) shared similar ^{16}O-rich sources of oxygen during initial petrogenesis; and 2) and underwent partial oxygen exchange under different conditions in different settings. The fine-grained CAI grew by accretion of fine-grained spinel ± melilite-bearing nodules that were held together in a matrix of very fine-grained Al-diopside. Spinel, Al-diopside, and forsterite in this CAI have retained their initial ^{16}O-rich isotopic compositions, and melilite has undergone variable isotopic exchange with a ^{16}O-poor oxygen reservoir. The fine-grain size of melilite and incomplete isotopic exchange indicates that this alteration event was relatively mild.

The coarse-grained CAI is a type B1 object with melilite zoning, mineral textures, and an assemblage indicative of crystallization of a single liquid droplet. Similar to many coarse-grained CAIs from CV chondrites, spinel and fassaite are ^{16}O-rich, and melilite is ^{16}O-poor. However, the anorthite in this CAI is ^{16}O-rich, unlike many CAIs from Allende (Clayton et al. 1977; Mayeda et al. 1986; Yurimoto et al. 1994). All of the melilite analyses from this CAI are ^{16}O-rich. This fact coupled with the coarse grain size of this CAI reflects a stronger, more pervasive isotope exchange event than the event that affected the fine-grained CAI. As the two CAIs were adjacent to each other on the parent body, the coarse-grained CAI must have been altered before its parent body history, most likely in a nebular setting. These results suggest that the widely observed ^{16}O-depletion in melilite from coarse-grained CAIs in the CV chondrites (Clayton 1993) is due to isotopic exchange in a nebular setting.

Editorial Handling—Dr. Ian Lyon

REFERENCES

Aléon J., Krot A. N., and McKeegan K. D. 2002. Calcium-aluminum-rich inclusions and amoeboid olivine aggregates from the CR carbonaceous chondrites. *Meteoritics & Planetary Science* 37: 1729–1755.

Clayton R. N. 1993. Oxygen isotopes in meteorites. *Annual Review of Earth and Planetary Sciences* 21:115–149.

Clayton R. N. 2002. Self-shielding in the solar nebula. *Nature* 415: 860–861.

Clayton R. N. 2004. The origin of oxygen isotope variations in the early solar system (abstract #1682). 35th Lunar and Planetary Science Conference. CD-ROM.

Clayton R. N. and Mayeda T. K. 1984. The oxygen isotope record in Murchison and other carbonaceous chondrites. *Earth and Planetary Science Letters* 67:151–166.

Clayton R. N., Grossman L., and Mayeda T. K. 1973. A component of primitive nuclear composition in carbonaceous meteorites. *Science* 182:485–488.

Clayton R. N., Onuma N., Grossman L., and Mayeda T. K. 1977. Distribution of the pre-solar component in Allende and other carbonaceous chondrites. *Earth and Planetary Science Letters* 34:209–224.

Clayton R. N., Mayeda T. K., Goswami J. N., and Olsen E. J. 1991. Oxygen isotope studies of ordinary chondrites. *Geochimica et Cosmochimica Acta* 55:2317–2337.

Davis A. M., MacPherson G. J., Clayton R. N., Mayeda T. K., Sylvester P. J., Grossman L., Hinton R. W., and Laughlin J. R. 1991. Melt solidification and late-stage evaporation in the evolution of a FUN inclusion from the Vigarano C3V chondrite. *Geochimica et Cosmochimica Acta* 55:621–637.

Ebel D. S. and Grossman L. 2000. Condensation in dust-enriched systems. *Geochimica et Cosmochimica Acta* 64:339–366.

Eiler J. M., Graham C., and Valley J. W. 1997. SIMS analysis of oxygen isotopes: Matrix effects in complex minerals and glasses. *Chemical Geology* 138:221–244.

Fagan T. J., McKeegan K. D., Krot A. N., and Keil K. 2001. Calcium-aluminum-rich inclusions in enstatite chondrites (II): Oxygen isotopes. *Meteoritics & Planetary Science* 36:223–230.

Fagan T. J., Krot A. N., and Yurimoto H. 2003. Petrology and oxygen isotope compositions of refractory inclusions from Acfer 094 (abstract #1288). 33rd Lunar and Planetary Science Conference. CD-ROM.

Fagan T. J., Krot A. N., Keil K., and Yurimoto H. 2004. Oxygen isotopic evolutoin of amoeboid olivine aggregates in the reduced CV3 chondrites Efremovka, Vigarano, and Leoville. *Geochimica et Cosmochimica Acta* 68:2591–2611.

Greenwood J. P. 2004. Disequilibrium melting of refractory inclusions: A mechanism for high-temperature oxygen isotope exchange in the solar nebula (abstract #2132). 35th Lunar and Planetary Science Conference. CD-ROM.

Greenwood J. P. and Hess P. C. 1996. Congruent melting kinetics: Constraints on chondrule formation. In *Chondrules and the protoplanetary disk,* edited by Hewins R. H., Jones R. H., and Scott E. R. D. Cambridge: Cambridge University Press. pp. 205–211.

Grossman L. 1972. Condensation in the primitive solar nebula. *Geochimica et Cosmochimica Acta* 36:597–619.

Guan Y., McKeegan K. D., and MacPherson G. J. 2000. Oxygen isotopes in calcium-aluminum-rich inclusions from enstatite chondrites: New evidence for a single CAI source in the solar nebula. *Earth and Planetary Science Letters* 181:271–277.

Harazono K. and Yurimoto H. 2003. Oxygen isotopic variations in a fluffy type A CAI from the Vigarano meteorite (abstract #1540). 34th Lunar and Planetary Science Conference. CD-ROM.

Imai H. and Yurimoto H. 2003. Oxygen isotopic distribution in an amoeboid olivine aggregate from the Allende CV chondrite: Primary and secondary processes. *Geochimica et Cosmochimica Acta* 67:765–772.

Ingrin J., Pacaud L., and Olivier J. 2001. Anisotropy of oxygen diffusion in diopside. *Earth and Planetary Science Letters* 192: 347–361.

Ito M., Yurimoto Y., and Nagasawa H. 1998. Oxygen isotope microanalysis of CAI by SIMS: An evidence for isotopically anomalous melilite (abstract #1556). 29th Lunar and Planetary Science Conference. CD-ROM.

Kim G. L., Yurimoto H., and Sueno S. 2002. Oxygen isotopic composition of a compound Ca-Al-rich inclusion from Allende meteorite: Implications for origin of palisade bodies and O-isotopic environment in the CAI forming region. *Journal of Mineralogical and Petrological Sciences* 97:161–167.

Kojima T., Tomeoka K., and Takeda H. 1993. Unusual dark clasts in the Vigarano CV3 carbonaceous chondrite: Record of parent body process. *Meteoritics* 28:649–658.

Kornacki A. S. and Wood J. A. 1985. Mineral chemistry and origin of spinel-rich inclusions in the Allende CV3 chondrite. *Geochimica et Cosmochimica Acta* 49:1219–1237.

Krot A. N., Petaev M. I., Scott E. R. D., Choi B. G., Zolensky M. E., and Keil K. 1998. Progressive alteration in CV3 chondrites: More evidence for asteroidal alteration. *Meteoritics & Planetary Science* 33:1065–1085.

Krot A. N., McKeegan K. D., Russell S. S., Meibom A., Weisberg M. K., Zipfel J., Krot T. V., Fagan T. J., and Keil K. 2001. Refractory calcium-aluminum-rich inclusions and aluminum-diopside-rich chondrules in the metal-rich chondrites Hammadah al Hamra 237 and Queen Alexandra Range 94411. *Meteoritics & Planetary Science* 36:1189–1216.

Krot A. N., McKeegan K. D., Leeshin L. A., MacPherson G. J., and Scott E. R. D. 2002. Existence of an ^{16}O-rich gaseous reservoir in the solar nebula. *Science* 295:1051–1054.

Lyons J. R. and Young E. D. 2004. Evolution of oxygen isotopes in the solar nebula (abstract #1970). 35th Lunar and Planetary Science Conference. CD-ROM.

MacPherson G. J. and Grossman L. 1981. A once-molten coarse-grained, Ca-rich inclusion in Allende. *Earth and Planetary Science Letters* 52:16–24.

MacPherson G. J., Krot A. N., Ulyanov A. A., and Hicks T. 2002. A comprehensive study of pristine, fine-grained, spinel-rich inclusions from the Leoville and Efremovka CV3 chondrites, I: Petrology (abstract #1526). 33rd Lunar and Planetary Science Conference. CD-ROM.

Mayeda T. K., Clayton R. N., and Nagasawa H. 1986. Oxygen isotope variations within Allende refractory inclusions (abstract). 17th Lunar and Planetary Science Conference. pp. 526–527.

McKeegan K. D. and Leshin L. A. 2001. Stable isotope variations in extraterrestrial materials. In *Stable isotope geochemistry,* edited by Valley J. W. and Cole D. R. Washington D.C.: Mineralogical Society of America. pp. 279–318.

McKeegan K. D., Leshin L. A., Russell S. S., and MacPherson G. J. 1998. Oxygen isotopic abundances in calcium-aluminum-rich inclusions from ordinary chondrites: Implications for nebular heterogeneity. *Science* 280:414–418.

McSween H. Y., Jr. 1977. Petrographic variations among carbonaceous chondrites of the Vigarano type. *Geochimica et Cosmochimica Acta* 41:1777–1790.

Meeker G. P., Wasserburg G. J., and Armstrong J. T. 1983. Replacement textures in CAI and implications regarding planetary metamorphism. *Geochimica et Cosmochimica Acta* 47: 707–721.

Petaev M. I. and Wood J. A. 1998. The condensation with partial isolation (CWPI) model of condensation in the solar nebula. *Meteoritics & Planetary Science* 33:1123–1137.

Russell S. S., Huss G. R., Fahey A. J., Greenwood R. C., Hutchison R., and Wasserburg G. J. 1998. An isotopic and petrologic study of calcium-aluminum-rich inclusions from CO3 meteorites. *Geochimica et Cosmochimica Acta* 62:689–714.

Ryerson F. J. and McKeegan K. D. 1994. Determination of oxygen self-diffusion in åkermanite, anorthite, diopside, and spinel: Implications for oxygen isotopic anomalies and the thermal histories of Ca-Al-rich inclusions. *Geochimica et Cosmochimica Acta* 58:3713–3734.

Sahijpal S., McKeegan K. D., Krot A. N., Weber D., and Ulyanov A. A. 1999. Oxygen-isotopic compositions of calcium-aluminum-rich inclusions from the CH chondrites, Acfer 182, and Patuxtent Range 91546 (abstract). *Meteoritics & Planetary Science* 34: A101.

Scott E. R. D. and Krot A. N. 2001. Oxygen isotopic compositions and origins of calcium-aluminum-rich inclusions and chondrules. *Meteoritics & Planetary Science* 36:1307–1319.

Shimizu N. and Hart S. R. 1982. Applications of the ion microprobe to geochemistry and cosmochemistry. *Annual Review of Earth and Planetary Sciences* 10:483–526.

Stolper E. 1982. Crystallization sequences of Ca-Al-rich inclusions from Allende: An experimental study. *Geochimica et Cosmochimica Acta* 46:2159–2180.

Thiemens M. H. 1999. Mass-independent isotope effects in planetary atmospheres and the early solar system. *Science* 283:341–345.

Thiemens M. H. and Heidenreich J. E., III. 1983. The mass-independent fractionation of oxygen: A novel isotope effect and its possible cosmochemical implications. *Science* 219:1073–1075.

Wark D. A. and Lovering J. F. 1977. Marker events in the early evolution of the solar system: Evidence from rims on Ca-Al-rich inclusions in carbonaceous chondrites. Proceedings, 8th Lunar and Planetary Science Conference. pp. 95–112.

Wasson J. T., Yurimoto H., and Russell S. S. 2001. ^{16}O-rich melilite in CO3.0 chondrites: Possible formation of common ^{16}O-poor melilite by aqueous alteration. *Geochimica et Cosmochimica Acta* 65:4539–4549.

Young E. D. and Lyons J. R. 2003. CO self shielding in the outer solar nebula: An astrochemical explanation for the oxygen isotope slope-1 line (abstract #1923). 34th Lunar and Planetary Science Conference. CD-ROM.

Young E. D. and Russell S. S. 1998. Oxygen reservoirs in the early solar nebula inferred from an Allende CAI. *Science* 282:452–455.

Yurimoto H., Morioka M., and Nagasawa H. 1989. Diffusion in single crystals of melilite: I. Oxygen. *Geochimica et Cosmochimica Acta* 53:2387–2394.

Yurimoto H., Oishi K., Nagasawa H., Yuasa H., and Shigeho S. 1991. Sector-zoned pyroxene in Allende CAI and the implications for oxygen isotope distribution (abstract). 16th Meeting on Antarctic Meteorites, National Institute of Polar Research. pp. 60–61.

Yurimoto H., Nagasawa H., Mori Y., and Matsubaya O. 1994. Micro-distribution of oxygen isotopes in a refractory inclusion from the Allende meteorite. *Earth and Planetary Science Letters* 128:47–53.

Yurimoto H., Ito M., and Nagasawa H. 1998. Oxygen isotope exchange between refractory inclusion in Allende and solar nebula gas. *Science* 282:1874–1877.

Yurimoto H. and Kuramoto K. 2002. A possible scenario introducing heterogeneous oxygen isotopic distribution in protoplanetary disks (abstract). *Meteoritics & Planetary Science* 37:A153.